

REPORT DOCUMENTATION PAGE				Form Approved OMB No. 0704-0188	
Public reporting burden for this collection of information is estimated to average 1 hour per response, including the time for reviewing instructions, searching existing data sources, gathering and maintaining the data needed, and completing and reviewing this collection of information. Send comments regarding this burden estimate or any other aspect of this collection of information, including suggestions for reducing this burden to Department of Defense, Washington Headquarters Services, Directorate for Information Operations and Reports (0704-0188), 1215 Jefferson Davis Highway, Suite 1204, Arlington, VA 22202-4302. Respondents should be aware that notwithstanding any other provision of law, no person shall be subject to any penalty for failing to comply with a collection of information if it does not display a currently valid OMB control number. <b>PLEASE DO NOT RETURN YOUR FORM TO THE ABOVE ADDRESS.</b>					
1. REPORT DATE (DD-MM-YYYY) 23-10-2008		2. REPORT TYPE Technical Paper		3. DATES COVERED (From - To)	
4. TITLE AND SUBTITLE  <b>On the Inner Jet Spread Angles of Coaxial Jets from Subcritical to Supercritical Conditions with Preliminary Numerical Results (Preprint)</b>				5a. CONTRACT NUMBER	
				5b. GRANT NUMBER	
				5c. PROGRAM ELEMENT NUMBER	
6. AUTHOR(S) Juan I. Rodriguez (UCLA); Jeffrey J. Graham, Ivett A. Leyva, & Douglas Talley (AFRL/RZSA); Hsin-Yuan Lyu (Advatech Pacific)				5d. PROJECT NUMBER	
				5e. TASK NUMBER 23080533	
				5f. WORK UNIT NUMBER	
7. PERFORMING ORGANIZATION NAME(S) AND ADDRESS(ES)  Air Force Research Laboratory (AFMC) AFRL/RZSA 10 E. Saturn Blvd. Edwards AFB CA 93524-7680				8. PERFORMING ORGANIZATION REPORT NUMBER  AFRL-RZ-ED-TP-2008-463	
9. SPONSORING / MONITORING AGENCY NAME(S) AND ADDRESS(ES)  Air Force Research Laboratory (AFMC) AFRL/RZS 5 Pollux Drive Edwards AFB CA 93524-7048				10. SPONSOR/MONITOR'S ACRONYM(S)	
				11. SPONSOR/MONITOR'S NUMBER(S) AFRL-RZ-ED-TP-2008-463	
12. DISTRIBUTION / AVAILABILITY STATEMENT  Approved for public release; distribution unlimited (PA #08419A).					
13. SUPPLEMENTARY NOTES For presentation at the 55 <sup>th</sup> JANNAF Propulsion/4 <sup>th</sup> LPS/3 <sup>rd</sup> SPS/6 <sup>th</sup> MSS Joint Meeting, to be held in Orlando, FL, 8-12 Dec 2008.					
14. ABSTRACT  A study is performed to analyze the behavior of the inner jet spread angles in a coaxial jet flow configuration similar to those used in liquid rocket engines. These angles are measured from back-lit images. Data is presented for sub-, near-, and supercritical non-reactive N2 coaxial jets. In the subcritical regime, the effects of an externally-imposed transverse acoustic field are also analyzed. The acoustic field is generated using two piezo-sirens and driven at a frequency of $3.0 \pm 0.1$ kHz. Pressure oscillations vary from 16 to 22 kPa, peak to peak, at the location of the jet with background pressure of 1.5 MPa. For all cases, by varying the inner and outer jet temperatures and mass flowrates, outer to inner jet velocity ratios from 0.25 to 23 and outer to inner jet momentum flux ratios (J) from 0.02 to 23 are achieved. In the case where no acoustic excitation is applied the angles for the near- and supercritical cases show more spread compared to their subcritical counterparts for $1.0 < J < 2.5$ , attaining values up to 18°. However, at higher J values, the spread angles for subcritical pressures are larger than those for near- and supercritical pressures. When acoustics are applied at subcritical pressures, the largest spread angles occur for $2 < J < 10$ , reaching values as high as 38°. Also, preliminary numerical results are presented for two supercritical cases with only one acoustic source present.					
15. SUBJECT TERMS					
16. SECURITY CLASSIFICATION OF:			17. LIMITATION OF ABSTRACT  SAR	18. NUMBER OF PAGES  19	19a. NAME OF RESPONSIBLE PERSON Dr. Douglas Talley
a. REPORT  Unclassified	b. ABSTRACT  Unclassified	c. THIS PAGE  Unclassified			19b. TELEPHONE NUMBER (include area code) N/A

# On the inner jet spread angles of coaxial jets from subcritical to supercritical conditions with preliminary numerical results (Preprint)

Juan I. Rodriguez<sup>†</sup>, Jeffrey J. Graham<sup>\*</sup>, Ivett A. Leyva<sup>\*</sup>, Hsin-Yuan Lyu<sup>‡</sup>, Douglas Talley<sup>\*</sup>

<sup>†</sup>University of California, Los Angeles, Los Angeles, CA 90095

<sup>\*</sup>Air Force Research Laboratory/RZSA Edwards AFB, CA 93524

<sup>‡</sup>Advatech Pacific, Inc., Redlands, CA 92374

## ABSTRACT

A study is performed to analyze the behavior of the inner jet spread angles in a coaxial jet flow configuration similar to those used in liquid rocket engines. These angles are measured from back-lit images. Data is presented for sub-, near-, and supercritical non-reactive N<sub>2</sub> coaxial jets. In the subcritical regime, the effects of an externally-imposed transverse acoustic field are also analyzed. The acoustic field is generated using two piezo-sirens and driven at a frequency of  $3.0 \pm 0.1$  kHz. Pressure oscillations vary from 16 to 22 kPa, peak to peak, at the location of the jet with background pressure of 1.5 MPa. For all cases, by varying the inner and outer jet temperatures and mass flowrates, outer to inner jet velocity ratios from 0.25 to 23 and outer to inner jet momentum flux ratios (J) from 0.02 to 23 are achieved. In the case where no acoustic excitation is applied the angles for the near- and supercritical cases show more spread compared to their subcritical counterparts for  $1.0 < J < 2.5$ , attaining values up to 18°. However, at higher J values, the spread angles for subcritical pressures are larger than those for near- and supercritical pressures. When acoustics are applied at subcritical pressures, the largest spread angles occur for  $2 < J < 10$ , reaching values as high as 38°. Also, preliminary numerical results are presented for two supercritical cases with only one acoustic source present.

## NOMENCLATURE

$J = \rho_{\text{outer}} u_{\text{outer}}^2 / \rho_{\text{inner}} u_{\text{inner}}^2$ , outer to inner jet momentum flux ratio

$VR = u_{\text{outer}} / u_{\text{inner}}$ , outer to inner jet velocity ratio

## INTRODUCTION

The general problem of mixing between two jets in a coaxial configuration has been studied for several decades. Chigier and Beer [1] provided a very detailed description of the near field in an air-air coaxial jet with different outer to inner velocity ratios, VR ( $\infty$ , 2.35, 1.17, 0.235, 0.117, 0.024). They explain the interactions of the recirculation zone setup by the inner jet wall and the subsequent mixing process between the two jets. The lower VR is the less the inner jet is affected by the recirculation zone and the more the outer jet is deflected and entrained by the inner jet. Vice versa when VR is high, the inner jet is more affected by the recirculation zone whose vortices deflect the inner jet toward the annular jet thus getting entrained. Ko et al. and Chan et al. [2-5] have also provided detailed studies of air-air coaxial jets discharging into stationary air. In their research the inner jet post thickness was kept to a minimum. They obtained pressure measurements and hot-wire and microphone spectra. These studies are concerned with the characterization of the flow structures (e.g. vortices) developed at different regions in the coaxial jets and also with similarity of the mean velocity, turbulence intensity and pressure profiles.

In terms of the growth rate of the inner or outer jets in a coaxial configuration, several studies have also been completed by different groups [6-9]. As a point of reference, these results are often compared to the growth of shear layers between two planar flows which has been well characterized by several authors. Brown and Roshko [10], proposed an equation for the growth rate of the shear layer for subsonic two-dimensional incompressible turbulent gas-gas flows. Papamoschou and Roshko [11] later proposed an equation for the growth of the visual thickness of the shear layer for sub- to supersonic two-dimensional turbulent mixing layers. Finally, Dimotakis [12] proposed an equation for the vorticity growth rate of a planar freejet. Chehroudi et al. [13] showed that for single jets at supercritical pressure and temperature, the spreading angle agrees quantitatively with that predicted by the works mentioned above.

which were derived for incompressible variable-density gas-gas jets. The data from the present study will be compared to the abovementioned body of work.

The particular interest on coaxial jets in this work springs from their wide application in liquid rocket injectors. For example, the SSME for the Shuttle and the Vulcan engines for the Ariane rocket use coaxial injectors. Furthermore, in this study we greatly expand the region of study as compared to previous results. We study one-phase and two-phase flows in sub to supercritical pressures. We solely use  $N_2$  for the inner and outer jets and the chamber flows. This is to have a single critical point. In previous studies by the same group [14-15] preliminary results were presented for the growth rate of the outer jet. It was found that the spreading angle was fairly constant ( $\sim 12^\circ$ ) for all cases studied, except for the case of gas-gas jets at subcritical pressures with  $J < 0.1$  where the angles varied from  $-4^\circ$  to  $5^\circ$ .

In the first part of the present study we look at the behavior of the inner jet with and without an externally-imposed transverse acoustic field. On the complex problem of combustion instabilities, which has plagued the development of liquid rocket engines practically since their inception, the interaction of an acoustic field with an injector flow is considered a unit physics problem. Therefore, the intent of this paper is to aid on the understanding of this unit problem. In our experimental setup, we use a rectangular test section and we excite the jet with a transverse acoustic field. A transverse mode on a rectangular chamber would be the equivalent of a tangential mode on a cylindrical chamber which is one of the most dangerous. Thus, in our current experimental configuration we have two acoustic drivers which allow us to change the phase of the acoustic field with respect to the fixed location of the coaxial jet injector. The spread angles that we obtain under acoustic perturbation could perhaps be used by a designer as a measure of the lateral spread expected from a single element under similar conditions. This would aid with designing the separation between elements if one does not want inter-element interactions.

The second part of this paper presents preliminary data on numerical simulations performed for the case of one-phase flows at supercritical conditions with and without acoustic excitation. In these simulations, only one acoustic source is modeled. This condition matches earlier experiments by our group where only one piezo-siren was used to produce an acoustic field within the chamber [16-17]. For this initial numerical study, temperature and species fields were compared with high-speed camera images and axial dark core length results for two experimental cases from the above references.

## EXPERIMENTAL SETUP

The experiments in this study were conducted at the Air Force Research Laboratory (AFRL) in Edwards Air Force Base, CA using the Cryogenic Supercritical Laboratory (EC-4) facility. The main chamber and the supporting systems of EC-4 are shown in Figure 1.

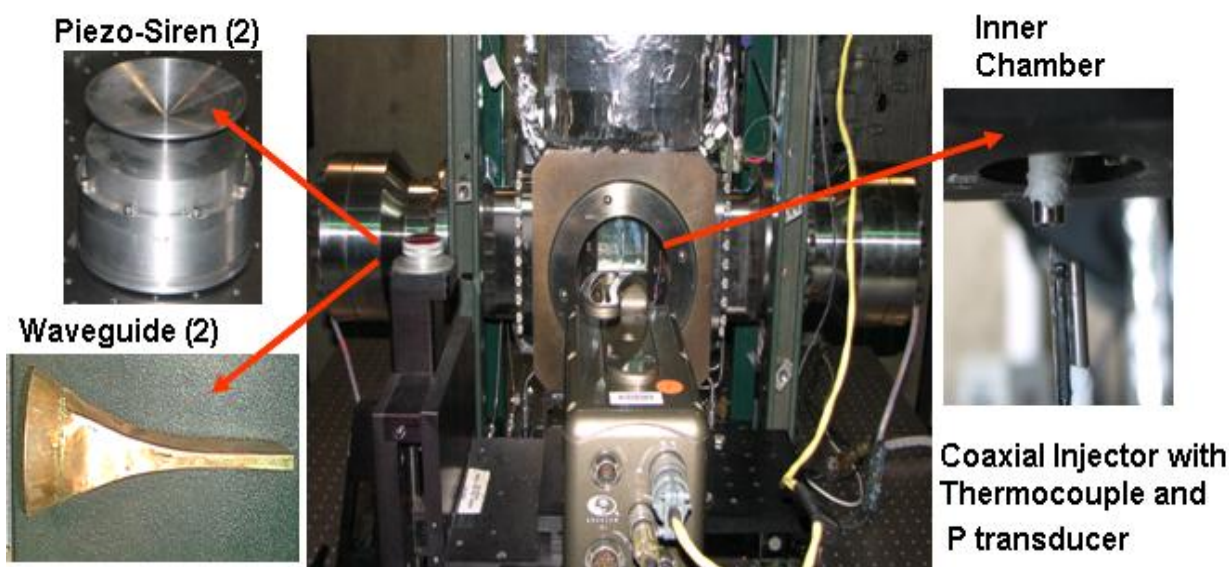


**Figure 1.** Overview of the experimental apparatus

Ambient temperature  $N_2$  is used to supply the inner and outer jet and also for chamber pressurization. Heat exchangers (HEs) using liquid nitrogen obtained from a cryogenic tank are used to cool the inner and the outer jets. One heat exchanger is used for the inner jet and two others for the outer jet. For the outer jet flow, the option to bypass one of the HEs to modify the cooling pattern is available. The temperature of the jets is controlled by the mass flow rate of liquid  $N_2$  through the HEs. To avoid difficulties with mass flow rate measurement at cryogenic temperatures, these rates are measured with Porter® mass flow meters (122 and 123-DKASVDAA) at ambient temperature. Both the inner and the outer jet flow through an injector assembly, shown in Fig. 2, which exits to an inner chamber built and housed inside the main chamber so that the amplitude of the acoustic oscillations is maximized at the test section. This inner chamber is 6.6 cm high, 7.6 cm wide and 1.3 cm deep (see image on the right in Fig. 1). A detailed image and dimensions of the coaxial injector tip are also found in Fig. 2. The tube housing the inner jet has an inner diameter,  $D_1$ , of 0.51 mm with length-to-diameter ratio of 100. The inner jet exit plane is recessed by 0.25 mm, or  $\frac{1}{2} D_1$ , from the outer jet. The outer annular jet's inner diameter,  $D_2$ , is 1.59 mm with outer diameter,  $D_3$ , of 2.42 mm. For the outer jet, the length-to-mean-width of the annular passage is 67.

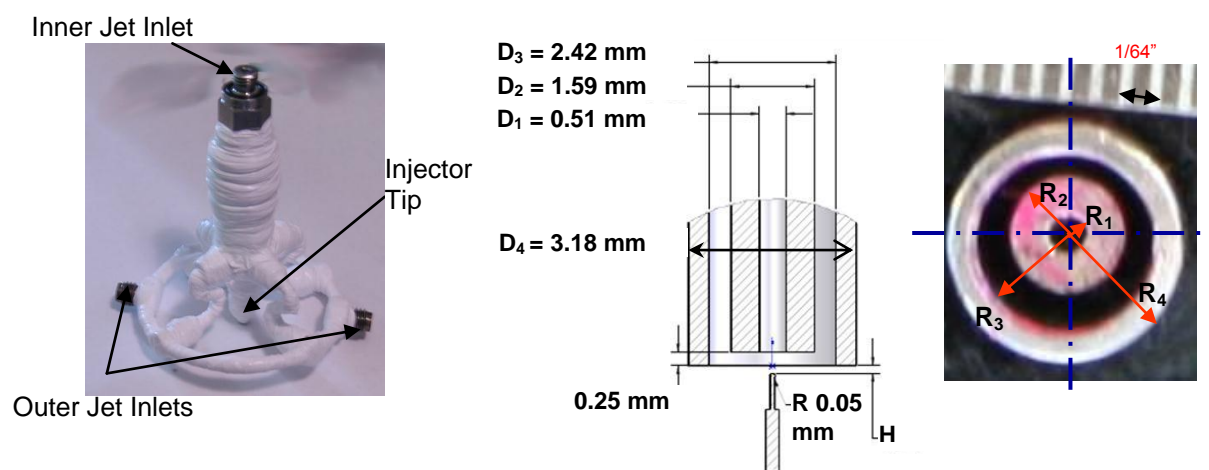


**Figure 2.** Image and tip geometry of the shear coaxial injector used in this study.

The temperature of the jets was measured using an unshielded type E thermocouple with a bead diameter of 0.1 mm. The accuracy of this thermocouple was checked with an RTD and found to be  $\pm 1$  K. The chamber pressure was measured with a Stellar 1500 transducer and a Kulite® XQC-062 pressure transducer. The latter was used to measure the pressure near the location of the thermocouple tip at a sampling frequency of 20 kHz (see rightmost picture in Fig. 1). Two linear positioning stages built by Attocube Systems AG were used to move the pressure transducer and the thermocouple in the plane perpendicular to the jet axis. Each stage has a range of about 3 mm in 1 dimension with step sizes in the order of 0.01 mm. One stage was placed on top of the other with their axis of movement perpendicular to each other for a total maximum examination area of 3 mm by 3 mm. The thermocouple and pressure transducer were fixed to a custom-made probe stand mounted on top of the positioning assembly. In turn, the linear stages were placed at the top end of a shaft that rested on a large 10-cm range linear stage built by SETCO™ outside the main chamber. Since the temperature probe approached the coaxial jet from the bottom and had sufficient range, it was capable of getting arbitrarily close to the exit plane of the coaxial jet. In fact, the thermocouple was even used to measure the temperature within the recess of the inner jet. The values for  $J$  and  $VR$  for a given condition were calculated using the measured flow rates, the mean chamber pressure and jet temperatures in conjunction with NIST's REFPROP® database [18-19]. Density, viscosity, and surface tension values were obtained from these properties.

Flow visualization was achieved with a Phantom® 7.1 CMOS camera. The camera can be seen facing the main chamber in the center picture of Fig. 1. Backlit images with a resolution from 128x200 to 192x400 pixels were obtained, with each pixel representing an area of approximately 0.08 mm by 0.08 mm. The framing rate was either 20 or 25 kHz. The number of images saved per run was 1000. The jet was backlit using a Newport® variable power arc lamp set at 160 W. The acoustic field for the subcritical

cases was generated using two piezo-sirens custom-designed by Hersh Acoustical Engineering, Inc. (see Fig. 1). An input sinusoidal voltage signal moves the piezoelectric element which has an aluminum cone attached to it producing acoustics waves. When the two drivers have a zero degree phase angle difference they move in opposite directions. Conversely, when the two drivers have a 180-degree phase difference the cones move in the same direction, ‘chasing’ each other. This behavior is represented by the sketches in Fig. 3. A Fluke® signal generator was used to drive the piezo-sirens with a sinusoidal wave at a chosen driving frequency and phase angle between them. The frequency was manually varied until the highest amplitudes of the pressure waves were obtained. These frequencies spanned a range between 2.96 and 3.06 kHz for the subcritical cases reported in this study. Then the signals were amplified and fed to the piezo-sirens keeping the voltage supplied to each driver constant. A waveguide with a catenary contour was used to guide the waves from a circular cross-section at the end of the aluminum cone to the rectangular cross-section of the inner chamber.

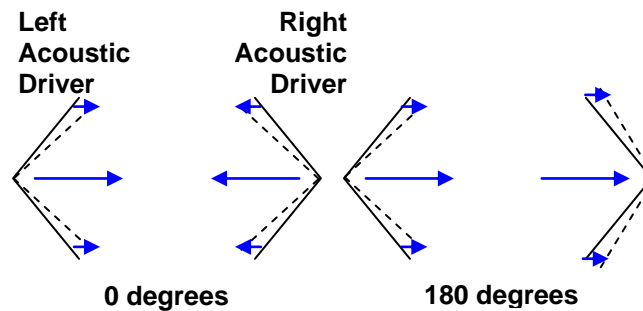


**Figure 3.** Simplified diagram of the two acoustic drivers at a 0° and 180° phase angle.

## EXPERIMENTAL RESULTS AND DISCUSSION

To obtain the inner jet spread angles for a given condition, 998 images such as the one shown in Fig. 4a were used. A raw image is converted to a black and white image using an image processing technique previously described in detail in Leyva et al. [16-17]. From the black and white image, a contour of the dark core is constructed as shown in Fig. 4c. We use the dark core to describe the behavior of the inner jet since for our experiments the inner jet is always colder, thus denser, than the outer jet and appears darker in the backlit images. In order to measure the two angles, first, the locations of the left and right contours were recorded for each image as pictured in Fig. 4d. Then, for each row, the leftmost and rightmost contour points from all 998 images were selected to build a “maximum left contour” and a “maximum right contour” as can be seen in Fig. 5.

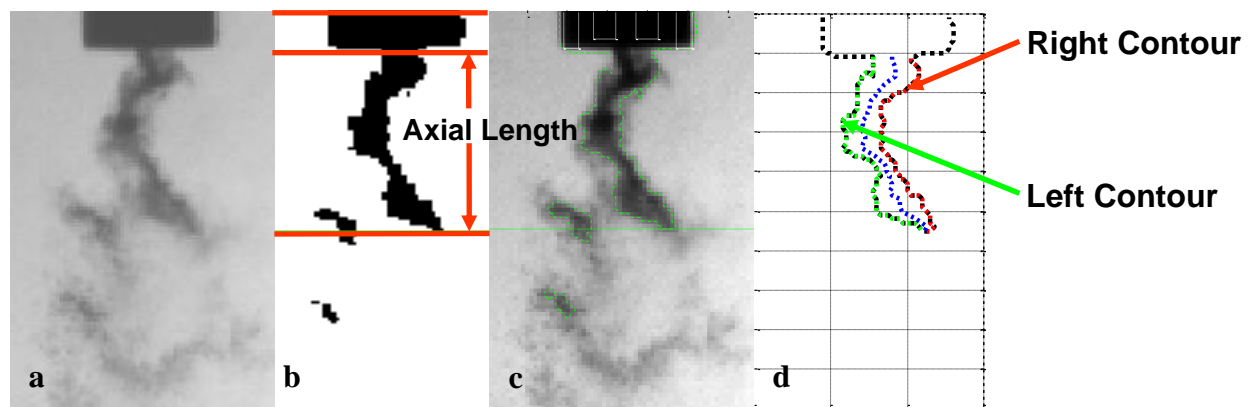


**Figure 4a.** Raw image from high-speed camera. **4b.** Black and white conversion after image processing. **4c.** Dark core boundary extracted from the processed black and white image. **4d.** Schematic of the left and right contours used in this study.

A linear fit through each contour was used to calculate the left and right spread angles. In Fig. 5 the two angles measured,  $\alpha_{\text{Left}}$  and  $\alpha_{\text{Right}}$ , are shown. The linear fit was chosen to start where the contour was the thinnest. This usually took place between  $\frac{1}{2} D_1$  (in supercritical cases at high Js, for example) up to  $5 D_1$  (for cases at moderate Js) and ended at the mean axial dark core length which is calculated by averaging the extracted axial length (see Fig. 4b) of all 998 images for each case. The axial dark core length is the axial projection of the dark core region connected to the injector and is also carefully explained in Leyva et al. [16-17]. An important reason for not choosing the first row of the contour to start the linear fit but begin a few inner jet diameters downstream was to avoid a recirculation zone that is generated due to the geometry of our injector. This recirculation occurs due to a thick inner jet post which prevents the inner jet and outer jet from coming into contact right away after the inner jet post ends. The recirculation region appears just as dark as the inner jet dark core and biases the measurements. By starting the linear fit where the contour is the thinnest we expect to avoid some of that bias.

Once the limits for the linear fit are chosen, a line is obtained and the angle associated with it is obtained. Both left and right angles computed in this manner are shown in Fig. 5. It is the sum of both left and right angles what is referred to in this study as the “inner jet spread angle”. This computed spread angle represents the region the inner jet traveled during the amount of time it took to record the 998 images. For the case of no acoustics, we call it ‘maximum baseline spread angle’. It is important to note that this ‘maximum baseline spread angle’ will over predict the mean of the spread angles. This is because we find the maximum contour out of all the images and then find a linear fit to the composite contour, instead of fitting a line and finding a spread angle for each image and then taking the average of those individual angles. When acoustics are present, this spreading angle encompasses a region where the inner jet traveled during all acoustic cycles captured in the number of images processed. Thus, for the cases where acoustics are on, this angle is referred to as the ‘maximum acoustic spread angle’.

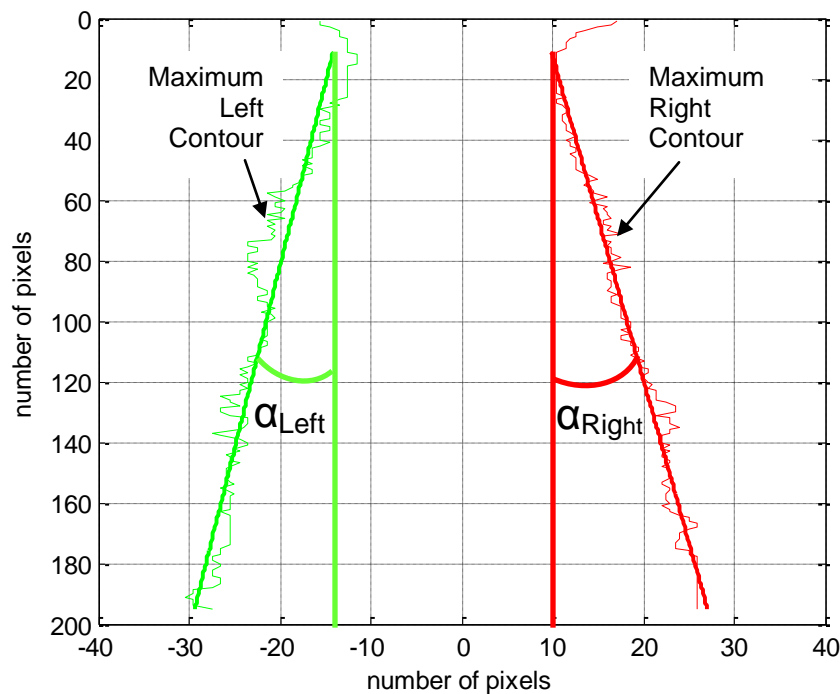


**Figure 5.** Left and right angles derived using the maximum displacement of the dark core at each row over a sample of 998 images.

Three values for the chamber pressure were selected for this study to span subcritical to supercritical values: 1.5 MPa, 3.6 MPa, and 4.9 MPa. For reference, the critical pressure,  $P_{\text{cr}}$ , of  $N_2$  is 3.39 MPa and its critical temperature,  $T_{\text{cr}}$ , is 126.2 K. At subcritical pressures, the inner jet reaches the saturation temperature while for near and supercritical pressures this temperature is kept as close as possible to the critical value.



## ANALYSIS OF SUBCRITICAL DATA WITH AND WITHOUT ACOUSTICS

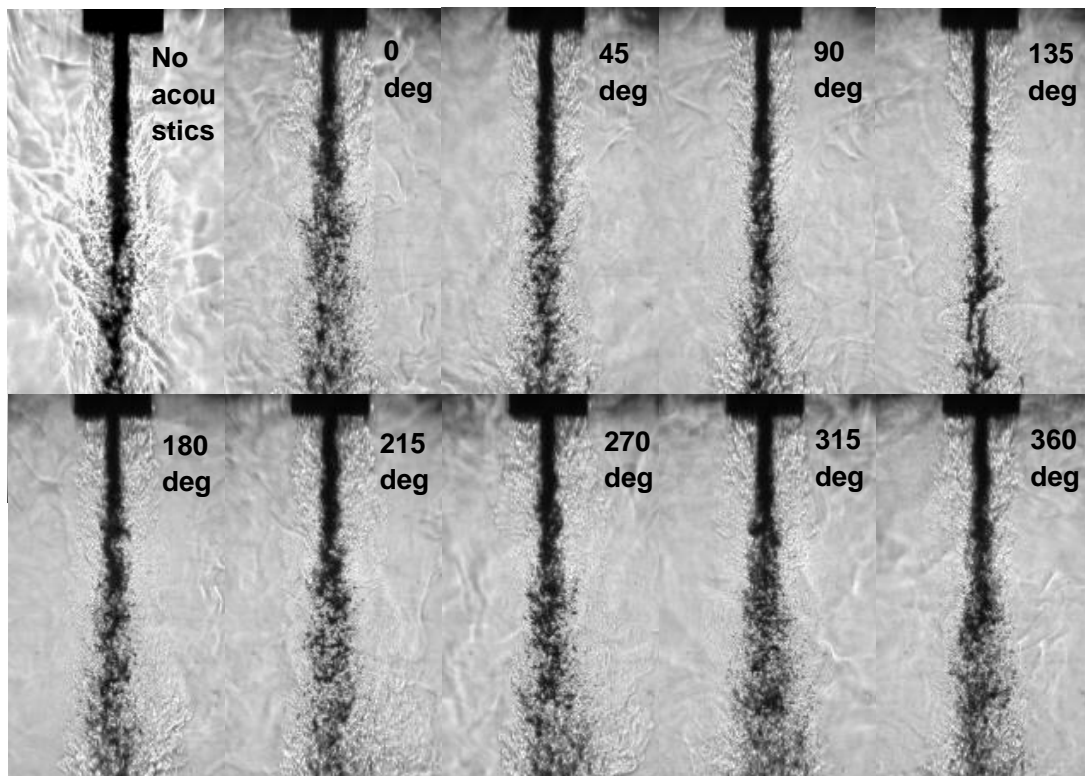


**Figure 6.** Collection of coaxial jet images at  $P_{\text{chamber}} = 1.50 \text{ MPa}$ ,  $J = 0.17$ .

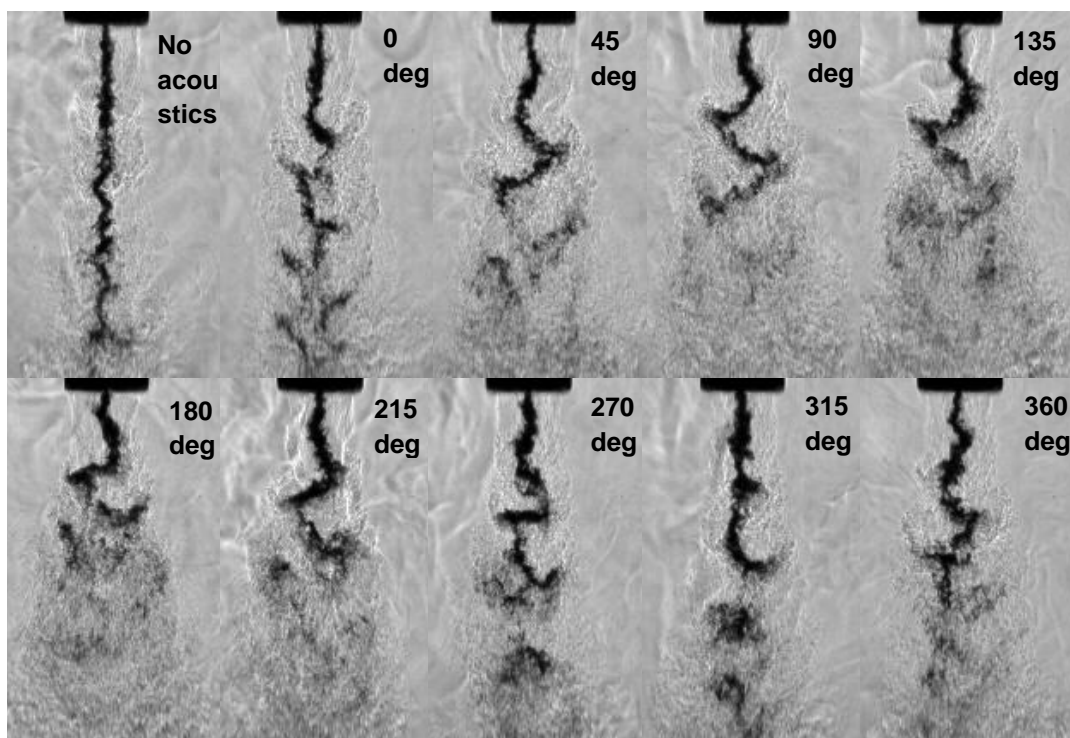


**Figure 7.** Collection of coaxial jet images at  $P_{\text{chamber}} = 1.45 \text{ MPa}$ ,  $J = 2.6$ .

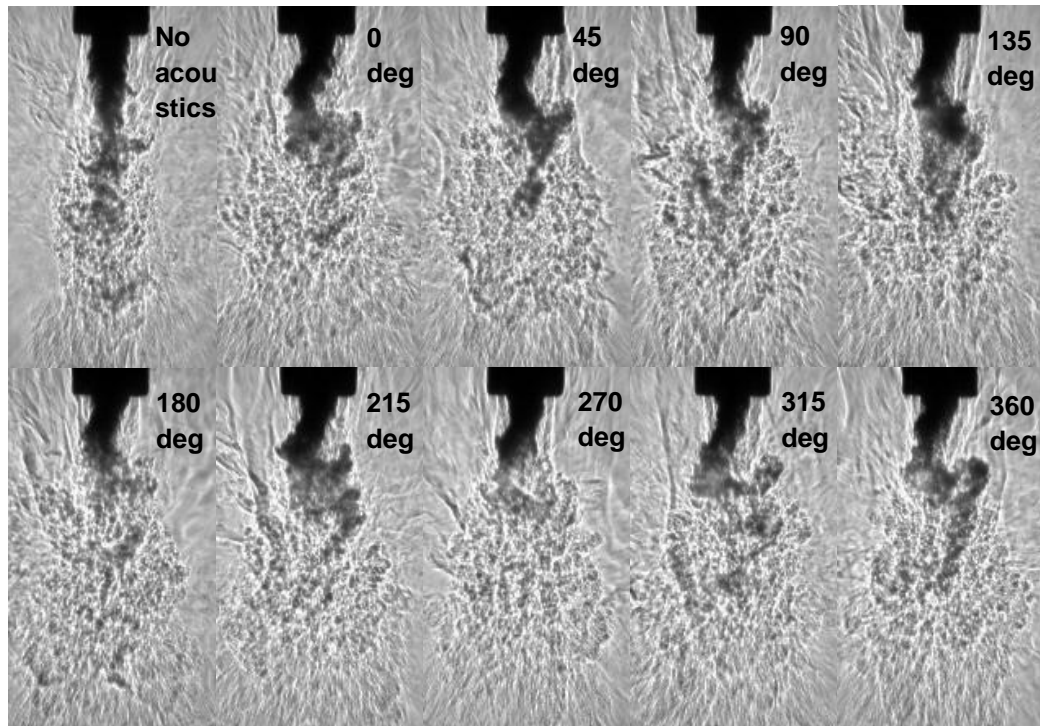


**Figure 8.** Collection of coaxial jet images at  $P_{\text{chamber}} = 1.50 \text{ MPa}$ ,  $J = 9.6$ .

A qualitative assessment of the coaxial jet flow at three different subcritical momentum flux ratios under acoustic excitation can be performed with the information shown in Figs. 6 to 8. In these figures the top left image represents the jet with no acoustics, a condition also referred throughout the paper as 'baseline', and the rest are images of the jet under different phase angles between the two piezo-sirens, varying in steps of  $45^\circ$  from  $0^\circ$  to  $360^\circ$ . The acoustic field generated produces maximum amplitudes over the chamber pressure,  $\Delta p/p$ , between 2.9 and 4.1%. The maximum spread angles, both baseline and acoustic, of all  $J$  values studied are compiled in Fig. 9.

At low momentum flux ratios the maximum spread angles are small. The images for  $J = 0.17$  in Fig. 6 as well as the upper-left plot in Fig. 9 show this behavior. For this case, the inner jet dominates the behavior of the coaxial jet, entraining and bending the outer jet towards itself. Since the inner jet in this case has a density of  $630 \text{ kg/m}^3$ , the outer jet and surrounding plenum have a density of  $27.7$  and  $22.0 \text{ kg/m}^3$  respectively, and both jets have similar mass flow rates around  $300 \text{ mg/s}$ , the flow surrounding the inner jet is simply not substantial enough to affect its behavior. When the acoustics are turned on, no discernable effect is seen, either visually in Fig. 6 or quantitatively in Fig. 9. This lack of a noticeable effect is also seen in previous observations made in terms of the decrease of the mean axial dark core length when acoustics are turned on [15, 20]. Acoustics in the range studied here do not seem to affect low  $J$  coaxial jets, neither by reducing the mean axial dark core length nor by increasing the maximum spread angles of the inner jet.

As we increase  $J$  to 1, one can start to observe a slight effect with phase angle (see upper-right plot in Fig. 9). Specifically, the maximum acoustic spread angle tends to achieve its largest value around a phase angle of  $180^\circ$ . This agrees with previous observations [15, 20] that the mean axial dark core length is reduced the most at or near a phase angle of  $180^\circ$ , which corresponds to a velocity antinode (pressure node). At  $J=2.6$ , the maximum acoustic spread angle increases continuously with phase angle reaching a maximum at a phase angle of  $180^\circ$  as shown in Figs. 7 and the middle-left plot in Fig. 9. In fact, the maximum acoustic spread angle recorded for this case at a phase angle of  $180^\circ$  is the one of highest from all cases at all phase angles. For the  $J=4.2$  case, we see a slight peak of the maximum acoustic spread angle at a phase angle of  $135^\circ$ , not far from the phase angle where we would expect the largest value which is  $180^\circ$ . Overall, we can conclude that for this range of  $J$ s, we observe the largest maximum acoustic spread angles when the jets are exposed to an acoustic field which has a velocity



antinode at the location of the jet (for our case, the two sources are  $180^\circ$  out of phase). These observations are expected to agree with previously shown results where the highest percentage of shrinkage of mean axial dark core length occurs for the same values of  $J$  since the data used to obtain those dark core length measurements is the same used to derive the maximum spread angles in this study [15].

As we move to the case where  $J=9.6$ , shown in Figs. 8 and the bottom-left plot in Fig. 9, we see a different behavior. In this case the inner jet achieves a uniformly high maximum acoustic spread angle, reaching a value as high as  $38^\circ$ , compared to its  $7^\circ$  maximum baseline spread angle. This large spreading occurs as long as there is a source of acoustic excitation. This behavior is irrespective of the different acoustic conditions produced by the change in phase angle, which produces no statistically relevant change upon its spreading properties. This is surprising since in previous studies [15, 20] we found that for  $J=9.6$  the percentage of shrinkage of the mean axial dark core length of the inner jet was smaller than for lower  $J$  values suggesting a smaller effect of acoustics on mixing. Also, in the aforementioned studies, we observed the mean axial dark core length change with phase angle whereas here the spread angle seems independent of phase. Finally as  $J$  increases to 23, we find a flatter profile of the maximum acoustic spread angle as the phase angle is varied. Also, all the values of maximum spread angles have decreased compared to the case of  $J=9.6$ . This is in agreement with previous results [15, 20] where it was found that for such high  $J$  values, the coaxial jet seems less sensitive to acoustic effects compared to moderate  $J$  values.

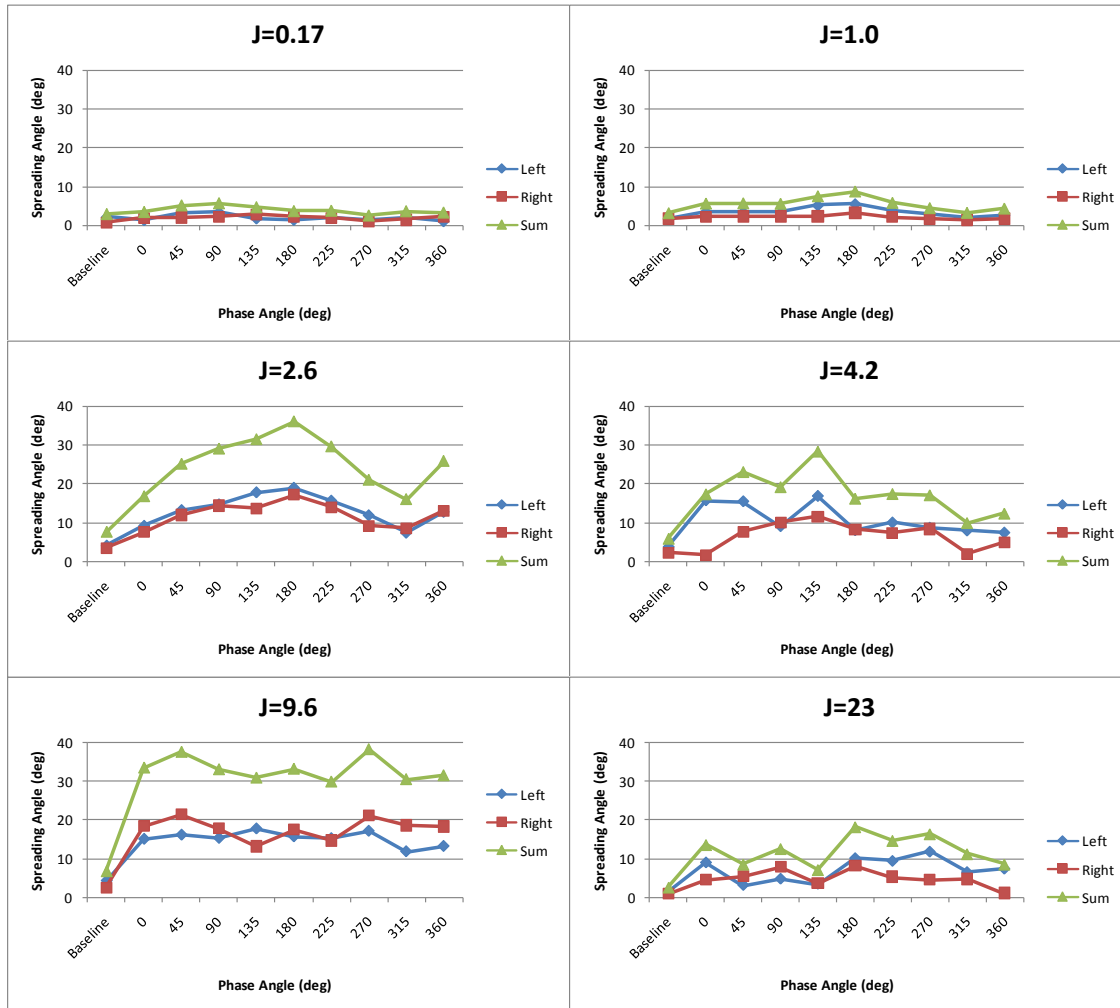


**Figure 9.** Maximum spread angles as a function of acoustic phase angle for different  $J$ s.

## ANALYSIS OF SUBCRITICAL TO SUPERCRITICAL DATA WITHOUT ACOUSTICS

Maximum baseline spread angles for all momentum flux ratios at the three pressure regimes were compared. It is important to remind the reader that this 'maximum baseline spread angle' over predicts the average of the spread angles for each image, as explained earlier in this section. However, because the jet is not being exposed to acoustics, the over prediction is expected to be small. The results for these baseline cases show that, for all pressures, as  $J$  increases, the maximum baseline spread angle first increases to a maximum value and then decays to similar or lower values than those observed for the lowest  $J$ s (see Fig. 10). The maximum baseline spread angles for the near- and supercritical cases show more variation than their subcritical counterparts which seem rather uniform for the  $J$  range studied. In addition, near- and supercritical pressures at  $1.0 < J < 2.5$  exhibit the largest maximum baseline spread angles, varying from  $14^\circ$  to  $18^\circ$ . At subcritical pressures the maximum baseline spread angles reach a maximum at  $J=2.6$ . Overall, two distinct trends are observed for the spread angles, one for subcritical (two-phase flow) and one for near and supercritical (one-phase flow) pressures.

Drawing a parallel between dark core lengths and spread angles, a long mean axial dark core length is indicative of slower mixing between the inner and the outer jet which also would result on a smaller maximum baseline spread angle for the inner jet. The trends for  $J < 2.5$  show that maximum baseline spread angles are larger for the near- and supercritical cases, support previous findings that, for a given  $J$ , the mean axial length of the inner jet dark core is larger for subcritical conditions than for near and supercritical conditions. However, at larger  $J$  values, the mean axial dark core lengths for the subcritical cases are larger than for the near- and supercritical cases which are counterintuitive to the results shown by the maximum baseline spread angles.

To put our results in context with the mixing layer growth of other well known flows such two-dimensional (2D) planar shear layers, we compared the current results to the theories given by Papamoschou and Roshko [11] and Dimotakis [12]. It was found that the maximum baseline spread angles measured for the conditions described here are larger than those estimated for 2D shear layers for the same density and velocity ratios. A 2D planar shear layer assumes contact between the inner jet and outer jet immediately after the boundary which separates them ends; however, our injector geometry features a thick inner jet post that creates a recirculation zone and delays the contact between the inner jet and the outer jet, which effectively blurs the discontinuity in velocity between the outer and inner jets. Thus, discrepancies were expected and confirmed by our results, which indicates that the differences between our current geometry and 2D shear layer flows are significant. Analogous theories to those provided by Papamoschou and Roshko [11] and Dimotakis [12] might be needed to better understand the class of flows described here.

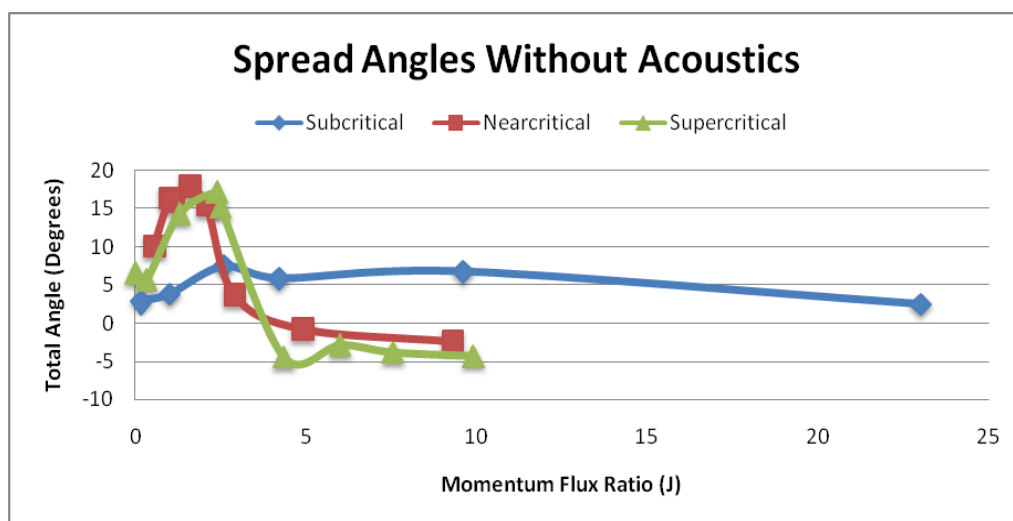


**Figure 10.** Maximum baseline spread angles as a function of momentum flux ratio for sub-, near-, and supercritical conditions.

## NUMERICAL RESULTS AND DISCUSSION

For the second part of the study, CFD++ of the Metacomp Technologies Inc. was used for the numerical simulations. CFD++ is capable of handling multi-physics phenomena encountered in a general fluid problem. For a detailed explanation of CFD++ capabilities please see CFD++ Manual [21]. The computational model considers compressible flow calculations. The 2-equation realizable  $k-\epsilon$  model was chosen for the turbulence modeling and a pre-conditioned pressure solver was used in the calculations. Spatial discretization is of second-order with a total variation diminishing limiter. Temporal discretization employs an implicit, dual time-stepping scheme, and a Riemann solver is used for the diffusion control. CFD++ provides an oscillating wall boundary condition, which may be used to simulate an acoustic driving source. Computational evaluation indicated that solutions of an acoustic cycle (about 0.3 ms) could be obtained within five hours of computational time on 48 AMD processors, which perform 64-bit operations.

We started the numerical simulations with a calculation of the acoustic field in a tube with one acoustic source and no jet present. The acoustic field for this simplified geometry has a known analytical solution. This calculation served to validate the acoustic capability of the computational tool, CFD++, used in the program. In addition, adjustments on the numerical settings and grid requirements could be optimized using this unit problem. For example, the longitudinal grid spacing (in the direction of the wave propagation) can be as large as 5 mm for frequencies ranging from 0.1 to 20 times the resonant frequency. Grid sizes in the transverse direction should not exceed 5 times that of the grid sizes in the longitudinal direction. Both the explicit and implicit time integration methods and both the pre-conditioned and non-pre-conditioned methods are effective for the acoustics modeling. The time step of one hundredth of a cycle proves to be acceptable. The unit problem exercise confirmed that the perturbation amplitudes should be small to avoid nonlinear effects. The limiting value of the perturbation amplitude for a linear acoustic wave depends on the acoustic frequency. Increased frequencies for a given amplitude leads to non-linear effects. Similarly, increased amplitudes for a given frequency lead to non-linear behavior.

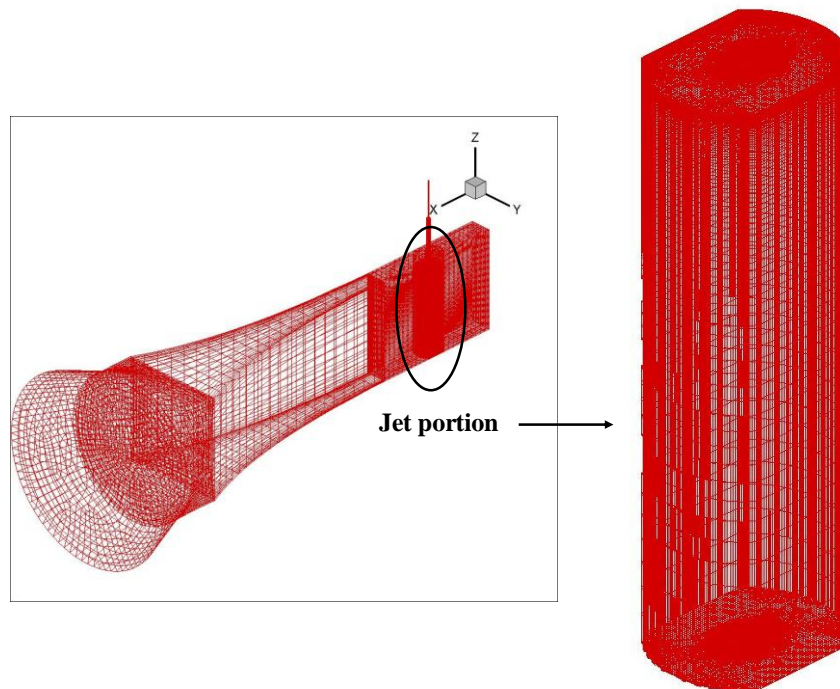


**Figure 11.** Grid for the Acoustic/Jet Calculations

After the unit problem calculations were complete, the next task was to introduce a jet into the simulation and use the actual 3D experimental geometry (including injector and chamber). We chose to simulate only one acoustic source for several reasons: 1) simplicity, 2) we also have data for that configuration, and 3) we want to understand the problem of one acoustic source well before we proceed to the more complex case of two acoustic sources. This also helped validate the supercritical models of CFD++. Grid issues and boundary condition representations were explored in the current study. A grid-independence analysis was performed and three numerical grids were constructed for the simulation. The grids had similar cell structure with different cell densities. One grid had 1.46 million cells, the other one had 2.06 million cells, and the final one had 3.32 million cells. Hybrid grids including both hexahedrals and tetrahedrals were used for the cells. The jet region required most cells; however, the grid density in the waveguide is sufficient judging from the experience learned in the acoustic unit problem calculations. Numerical tests showed that all three grids give satisfactory results; however, the 2.06-million-grid was used for most of the calculations (see Fig. 11).

The grid was first tested with an acoustic-only calculation (no jet) to examine the pressure mode-shapes. The results are shown in Fig. 12 where the position of the jet is noted with respect to the pressure field. The pressure fluctuations are accentuated as the acoustic field approaches the location of the coaxial jet. The reason for this enhancement in acoustic excitation is greatly due to the geometry that is used. As the waveguide that appears on the bottom left of Figs. 1 and its computer mesh model in Fig. 11 decreases in cross-sectional area, higher pressure fluctuations are possible. For each acoustic/jet calculation, a steady state solution with no acoustics was sought first, and enough iterations were used to assure the residues dropped three orders of magnitude. The velocity perturbation amplitude used in the boundary condition to simulate the acoustic wave was adjusted to match the experimental probing pressure at the jet exit. The flow Courant number was set to be 250. To cope with the near- or supercritical fluids, the Relich-Kwong-Soave equation of the state was used to describe the real gas behavior. In addition, the thermodynamic properties of nitrogen were extracted from the NIST database and curve-fitted into polynomials, illustrated in Fig. 13, which were then used in CFD++. This is because such curve fits were more accurate than the standard equations provided by the CFD++ user interface.

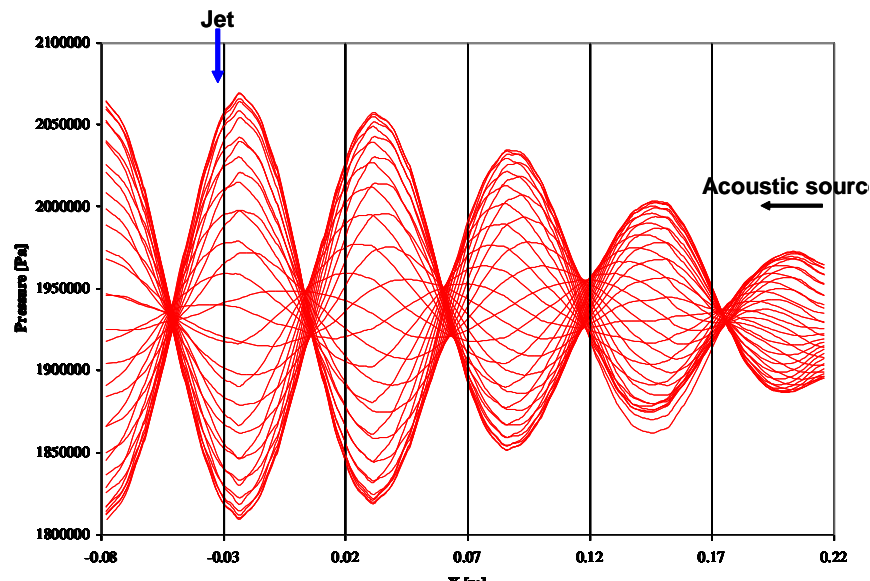


**Figure 12.** Pressure Mode Shape in the Experimental Geometry

Once the grid was tested, two supercritical cases were analyzed using the numerical model just described. The results are summarized in Table 1 below and shown in Figs. 14 and 15. Case SP2 has  $J = 1.3$  and  $VR = 1.8$ ,  $P_{\text{chamber}} = 4.93 \text{ MPa}$ ,  $T_{\text{chamber}} = 251 \text{ K}$ ,  $T_{\text{inner jet}} = 137 \text{ K}$ ,  $T_{\text{outer jet}} = 173 \text{ K}$ ,  $\dot{m}_{\text{inner jet}} = 291 \text{ mg/s}$ ,  $\dot{m}_{\text{outer jet}} = 2800 \text{ mg/s}$ . The frequency of the acoustic field was 3.11 kHz. SP6 has  $J = 3.7$  and  $VR = 3.27$ ,

$P_{\text{chamber}}=4.92\text{MPa}$ ,  $T_{\text{chamber}}=232\text{K}$ ,  $T_{\text{inner jet}}=136\text{K}$ ,  $T_{\text{outer jet}}=185\text{K}$ ,  $\dot{m}_{\text{inner jet}}=295\text{ mg/s}$ ,  $\dot{m}_{\text{outer jet}}=4240\text{ mg/s}$ . The acoustic frequency is 3.22 kHz. The reason that preliminary simulations of the coaxial jet experiment started with supercritical cases was the lack of a suitable two-phase model for the working fluid.

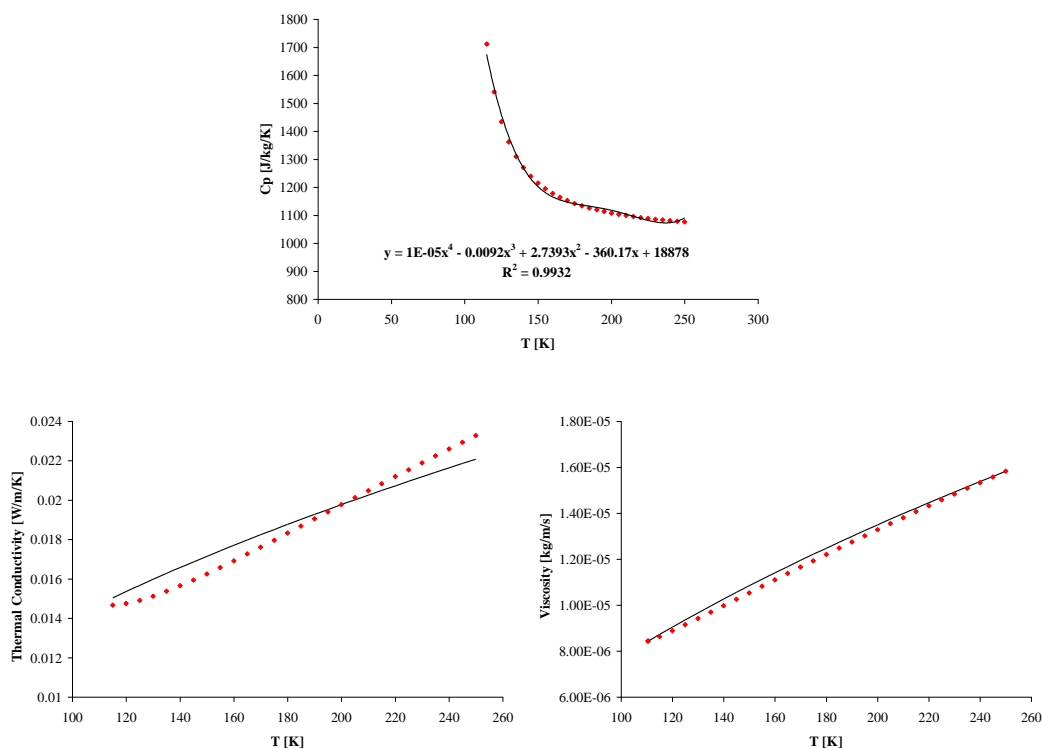


**Figure 13.** Polynomial curve-fitting of nitrogen transport properties from the NIST database.

The length of the inner jet is defined as the length of the region from the injector exit until an increment of 10% of the temperature difference between the inner and outer jets is achieved. This definition is arbitrary but it intends to capture the cold core of the inner jet. Using the temperature profile shown in the bottom row of Figs. 14 and 15, the numerical results produce a small inner jet core length for the SP6 case which is about one-sixth of that for the SP2 case. Observe that the agreement between the mean axial dark core length (from experimental results) and the numerical simulation for SP2 is encouraging. While the agreement is not as good for the higher J case, we can still see that these preliminary numerical results follow the general trend observed experimentally where the mean axial dark core length of the inner jet decreases with increasing momentum flux ratio.

**Table 1.** Summary of supercritical cases explored numerically.

Case	Inner Jet Core Length with no acoustics [L/D1] (Based on Temperature)	Pressure Fluctuations [kPa] (Peak-to-Peak at Jet Exit)	Dark Core Length with no acoustics [L/D1] (Experimental Results)
SP2 (J = 1.3)	5.5	~ 14	4.9
SP6 (J = 3.7)	1.0	~ 8.3	3.5



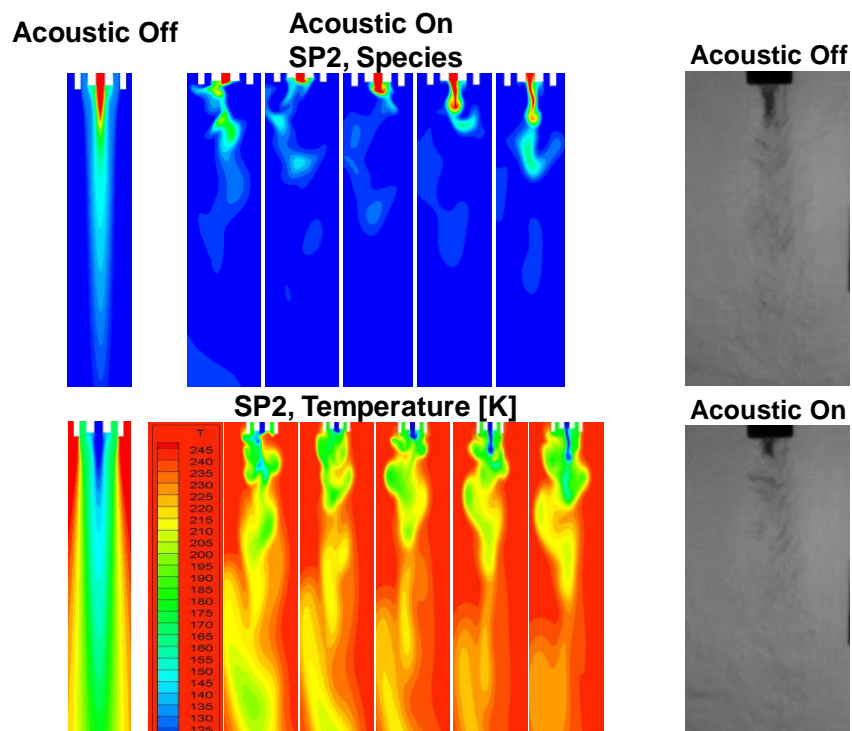


**Figure 14.** Numerical species concentration and temperature field at different instants and experimental images for condition SP2 with acoustics on and off.

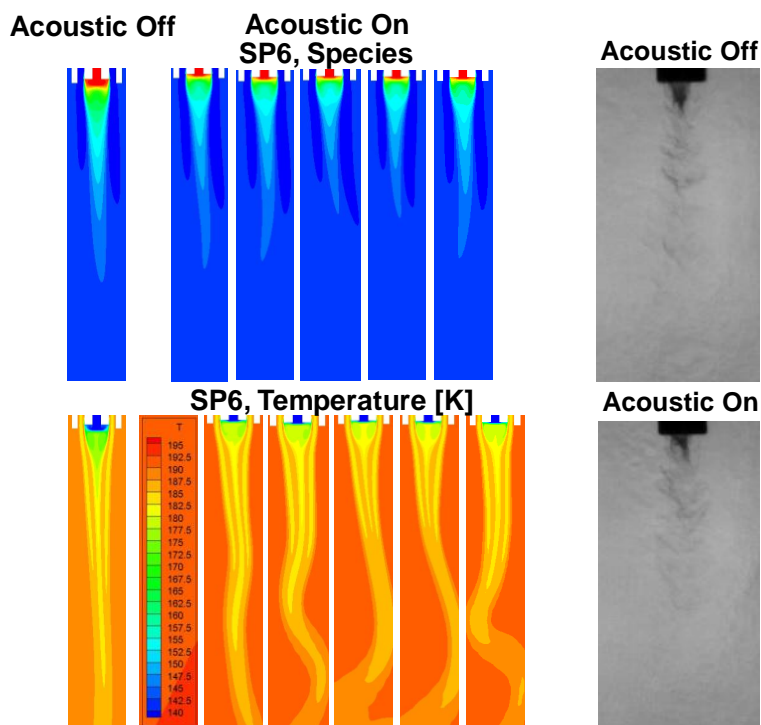


**Figure 15.** Numerical species concentration and temperature field at different instants and experimental images for condition SP6 with acoustics on and off.

Another trend that is supported by experimental evidence and it is observed in the numerical results is the decrease of the inner jet or dark core length when it is exposed to an external acoustic field. Both cases show a noticeable decrease in the dark core lengths as defined by the species concentration and the temperature field with the presence of acoustics. It is also noteworthy that the baseline conditions for both the SP2 and SP6 cases show very symmetric species and temperature fields, especially if they are compared to their respective behavior when acoustics are modeled. The oscillating patterns observed in both cases when acoustics are present agree very well in a qualitative sense with the type of phenomena observed experimentally when the jets are exposed to these levels of acoustic perturbations.

## CONCLUSIONS

The spread angles based on the maximum displacement of the inner jet dark core for a coaxial flow configuration were studied experimentally as a function of the chamber pressure and outer to inner jet momentum flux ratio. The experimental data used for this study had been previously reported in references 14-17, 20. However, previous analysis was mostly concerned with inner jet dark core lengths. The jet is either unexcited or under the influence of a transverse external acoustic field at approximately 3 kHz. When comparing the results with no acoustics at different pressures, the spread angles for the near- and supercritical cases were very similar to each other and showed more variation than their subcritical counterparts over the range of  $J$  values studied. We observe two distinct trends for the spread angles, one for subcritical (two-phase flow) and one for near and supercritical (one-phase flow) pressures. For these non-acoustic cases, all spread angles increase with  $J$  reaching a maximum around  $1 < J < 3$ . The largest spread angle recorded for a non-forced case was  $18^\circ$ .

For the cases with acoustic excitation, only subcritical pressures were studied. It was found that acoustics had either no effect or a slight effect on the spread angles for  $J$  up to 1. At moderate  $J$ 's ( $2 < J < 10$ ) an increase in the spread angle of  $30^\circ$  over the baseline was observed. For  $J=2.6$ , the spread angle reached a maximum when the phase angle between acoustic resonators was  $180^\circ$ , which corresponds to a velocity antinode, where the highest velocity fluctuations occur. This finding agrees with previous results which also looked at the effect of phase angle on the shrinkage of the inner jet dark core length. For  $J = 9.6$ , the spread angles show a similar response to the acoustic excitation, regardless of the phase angle between acoustic resonators, which is about 4 to 5 times the value from the non-acoustic baseline behavior. For  $J=23$ , the absolute acoustic spreading angles decrease but the percentage increase compared to the baseline is still in the order of 4 to 6 times growth.

Preliminary numerical results were presented for two cases at supercritical pressures. The agreement for the dark core length, albeit defined differently for the numerical and experimental cases, was within 10% for one case. Also, the numerical simulations show the experimental trends of decreased dark core length with both increasing  $J$  and also when acoustics are present for a given value of  $J$ .

## ACKNOWLEDGEMENTS

The authors would like to thank Randy Harvey for his very important contributions on running and maintaining the facility. This work is sponsored by AFOSR under Mitat Birkan, program manager.

## REFERENCES

1. Chigier, N. A., Beer, J. M., 'The flow region near the nozzle in double concentric jet', Transactions of the American Society of Mechanical Engineers, Journal of Basic Engineering, Vol. 86, pp 797-804, 1964.
2. Ko, N. W. M., Kwan, S. H., 'The initial region of subsonic coaxial jets', JFM, Vol. 73, part 2, pp. 305-332, 1976.
3. Ko, N. W. M., Chan, W. T., 'The inner regions of annular jets', JFM, Vol. 93, pp. 549-584, 1979.
4. Ko, N. W. M., Au, H., 'Coaxial jets of different mean velocity ratios', J. of Sound and Vibration, 1985, 100 (2), pp. 211-232.

5. Chan, W.T., Ko, N. W. M., 'Coherent structures in the outer mixing region of annular jet', JFM, Vol. 89, pp. 515-533, 1978.
6. Mayer W. O. H., Branam, R., 'Atomization characteristics on the surface of a round liquid jet', Exp. in Fluids, 36 (2004), pp. 528-539.
7. Favre-Marinet, M., Camano Schettini, E.B., "The density field of coaxial jets with large velocity ratio and large density differences", Int. J. of Heat and Mass Transfer, 44 (2001), pp. 1913-1924.
8. Ko, N. W. M., Au, H., "Initial region of subsonic coaxial jets", J of Fluids Engineering, June 1981, vol. 103, pp. 335-338.
9. Durao, D. and Whitelaw, J. H. Turbulent mixing in the developing region of coaxial jets", J of Fluids Engineering, Sept. 1973, pp. 467-473.
10. Brown, G., Roshko, A., "On density effects and large structure in turbulent mixing layers"; J. Fluid Mech, Vol. 64 part 4, 1974, pp. 775-816.
11. Papamoschou D., Roshko, A., "The compressible turbulent shear layer:an experimental study," J. Fluid Mech. Vol. 197, No. 453, 1988.
12. Dimotakis, P. E., "Two-Dimensional Shear Layer Entrainment", AIAA Journal, Vol 24, No. 11, Nov. 1986, pp. 1791-1796.
13. Chehroudi, B., Talley, D., Coy, E., "Visual characteristics and initial growth rates of round cryogenic jets at subcritical and supercritical pressure", Physics of Fluids, Vol. 14, No. 2, February 2002, pp. 851-861.
14. Leyva, I. A., Rodriguez, J. I., Chehroudi, B., Talley, D., "Preliminary Results on Coaxial Jets Spread Angles and the Effects of Variable Phase Transverse Acoustic Fields", AIAA-2008-0950.
15. Rodriguez, J. I., Leyva, I. A, Chehroudi, B., Talley, D., "Results on Subcritical One-Phase Coaxial Jet Spread Angles and Subcritical to Supercritical Acoustically-Forced Coaxial Jet Dark Core Lengths", AIAA-2008-4561.
16. Leyva, I. A., Chehroudi, B., Talley, D., "Dark-core analysis of Coaxial Injectors at Sub-, Near-, and Supercritical Conditions in a Transverse Acoustic Field", 54th JANNAF Meeting, Denver, CO, May 14-18, 2007.
17. Leyva, I. A., Chehroudi, B., Talley, D., "Dark-core analysis of Coaxial Injectors at Sub-, Near-, and Supercritical Conditions in a Transverse Acoustic Field", AIAA-2007-5456.
18. REFPROP, Reference Fluid Thermodynamic and Transport Properties, Software Package, Ver. 7.0, NIST, U.S. Department of Commerce, Gaithersburg, MD, 2002.
19. Thermophysical Properties of Fluid Systems (<http://webbook.nist.gov/chemistry/fluid>), NIST, U.S. Department of Commerce, Gaithersburg, MD, 2005.
20. Leyva, I. A., Rodriguez, J., Chehroudi, B., Talley, D., "Effect of Phase Angle on Coaxial Jet Behavior Spanning Sub- To Supercritical Pressures", Paper 14-2, 22nd European Conference on Liquid Atomization and Spray Systems, Como, Italy, September 8-10, 2008.
21. CFD++ User's Manual, Metacomp Technologies Inc, Agoura Hills, CA, 2008.

## APPENDIX

### A. Data Summary for Subcritical Cases

	$T_{\text{chamber}}$ (K)	$\rho_{\text{chamber}}$ (kg/m <sup>3</sup> )	$P_{\text{chamber}}$ (MPa)	$T_{\text{outer}}$ (K)	$\dot{m}_{\text{outer}}$ (mg/s)	$\rho_{\text{outer}}$ (kg/m <sup>3</sup> )	$u_{\text{outer}}$ (m/s)	$T_{\text{inner}}$ (K)	$\dot{m}_{\text{inner}}$ (mg/s)	$\rho_{\text{inner}}$ (kg/m <sup>3</sup> )	$u_{\text{inner}}$ (m/s)	Freq. (kHz)	VR
	Spreading Angles											$P'_{\text{RMS}}$	J
	Baseline	$\phi=0^\circ$	$\phi=45^\circ$	$\phi=90^\circ$	$\phi=135^\circ$	$\phi=180^\circ$	$\phi=225^\circ$	$\phi=270^\circ$	$\phi=315^\circ$	$\phi=360^\circ$			
<b>SUB</b>													
sub1	233	22.0	1.50	191	310	27.7	4.30	109	279	630	2.2	2.98	2.0
Left	2.2	1.4	3.0	3.4	1.8	1.5	1.9	1.5	2.1	1.1			
Right	0.8	2.0	2.1	2.2	2.8	2.2	1.9	1.0	1.5	2.2		21.5	0.17
sub2	231	22.2	1.50	183	790	28.8	11.0	109	283	630	2.2	3.06	4.8
Left	1.6	3.5	3.4	3.3	5.2	5.5	3.7	2.8	1.9	2.6			
Right	1.6	2.2	2.4	2.4	2.4	3.2	2.2	1.7	1.4	1.8		20.1	1.0
sub3	226	21.9	1.45	183	1230	27.8	16.9	109	284	630	2.2	3.06	7.6
Left	4.1	9.2	13.2	14.7	17.7	18.9	15.6	11.9	7.4	12.8			
Right	3.4	7.5	11.8	14.3	13.6	17.1	13.9	9.1	8.5	13.0		17.8	2.6
sub4	226	22.9	1.51	185	1560	28.7	20.9	109	279	630	2.2	2.96	9.5
Left	3.8	15.7	15.5	9.1	16.8	8.1	10.0	8.7	8.0	7.4			
Right	2.1	1.6	7.6	10.1	11.5	8.2	7.4	8.4	2.0	4.9		15.7	4.2
sub5	210	24.9	1.50	182	2400	29.3	31.3	109	279	630	2.2	3.01	14
Left	4.2	14.9	16.0	15.2	17.6	15.6	15.1	17.0	11.7	13.1			
Right	2.5	18.4	21.4	17.7	13.2	17.5	14.7	21.0	18.6	18.2		16.9	9.6
sub6	216	24.1	1.50	191	3640	27.7	50.3	109	279	630	2.2	3.02	23
Left	1.5	9.0	3.1	4.8	3.4	10.1	9.4	11.8	6.5	7.4			
Right	0.9	4.5	5.3	7.7	3.6	8.0	5.2	4.5	4.6	1.1		16.3	23

## B. Data Summary for Nearcritical Cases

	$T_{\text{chamber}}$ (K)	$\rho_{\text{chamber}}$ (kg/m <sup>3</sup> )	$P_{\text{chamber}}$ (MPa)	$T_{\text{outer}}$ (K)	$\dot{m}_{\text{outer}}$ (mg/s)	$\rho_{\text{outer}}$ (kg/m <sup>3</sup> )	$u_{\text{outer}}$ (m/s)	$T_{\text{inner}}$ (K)	$\dot{m}_{\text{inner}}$ (mg/s)	$\rho_{\text{inner}}$ (kg/m <sup>3</sup> )	$u_{\text{inner}}$ (m/s)	VR
	Spreading Angles Baseline											J
<b>NEAR</b>												
near1	223	56.6	3.58	180	1060	75.4	5.38	123	290	520	2.8	2.0
Left	4.8											
Right	5.3											0.55
near2	207	62.0	3.57	152	1570	101	5.95	117	289	590	2.4	2.5
Left	7.1											
Right	9.2											1.0
near3	228	55.1	3.58	185	1590	72.4	8.40	126	293	440	3.3	2.6
Left	4.6											
Right	11.4											1.1
near4	223	56.1	3.55	184	2170	72.3	11.5	127	294	360	4.0	2.8
Left	8.9											
Right	9.0											1.6
near5	230	54.2	3.56	199	2120	65.1	12.5	126	292	440	3.3	3.8
Left	2.1											
Right	13.4											2.1
near6	229	54.5	3.56	183	2690	73.1	14.1	126	292	420	3.4	4.1
Left	1.0											
Right	2.7											2.9
near7	219	57.6	3.56	194	3080	67.4	17.5	125	289	480	3.0	5.9
Left	-0.4											
Right	-0.5											4.9
near8	213	59.6	3.56	192	6460	68.3	36.2	128	295	220	6.6	5.5
Left	-4.1											
Right	1.6											9.3



### C. Data Summary for Supercritical Cases

	$T_{\text{chamber}}$ (K)	$\rho_{\text{chamber}}$ (kg/m <sup>3</sup> )	$P_{\text{chamber}}$ (MPa)	$T_{\text{outer}}$ (K)	$\dot{m}_{\text{outer}}$ (mg/s)	$\rho_{\text{outer}}$ (kg/m <sup>3</sup> )	$u_{\text{outer}}$ (m/s)	$T_{\text{inner}}$ (K)	$\dot{m}_{\text{inner}}$ (mg/s)	$\rho_{\text{inner}}$ (kg/m <sup>3</sup> )	$u_{\text{inner}}$ (m/s)	VR
	Spreading Angles											J
	Baseline											
<b>SUPER</b>												
super1	231	76.1	4.96	198	292	93.9	1.19	136	291	300	4.8	0.25
Left	3.5											
Right	3.1											0.019
super2	231	76.1	4.96	193	997	97.7	3.90	130	292	460	3.1	1.2
Left	3.8											
Right	2.0											0.33
super3	221	80.4	4.95	180	2050	109	7.19	128	291	490	2.9	2.5
Left	8.2											
Right	6.3											1.3
super4	222	80.1	4.96	182	3110	107	11.1	134	288	360	3.9	2.8
Left	6.3											
Right	11.0											2.4
super5	222	80.3	4.97	191	2820	99.5	10.8	131	293	440	3.3	3.3
Left	3.5											
Right	11.8											2.5
super6	236	73.79	4.94	195	5753	96	23	147	295	179	8.1	2.9
Left	-2.0											
Right	-2.4											4.4
super7	225	79	4.94	183	5813	107	20.9	138	295	264	5.5	3.9
Left	0.0											
Right	-2.9											6.0
super8	236	73	4.89	188	7055	100	26.9	141	293	214	6.76	4.0
Left	0.0											
Right	-3.8											7.6
super9	211	85.8	4.96	187	5820	103	21.6	132	286	410	3.4	6.3
Left	-3.0											
Right	-1.3											9.9